The Study of Nondestructive Analysis for Archaeological Samples Using High Energy Synchrotron Radiation and Laser Electron Photons

(高エネルギー放射光とレーザー電子光を用いた考古遺物に対する非破壊分析手法の研究)

佐藤 泰

The Study of Nondestructive Analysis for Archaeological Samples Using High Energy Synchrotron Radiation and Laser Electron Photons

SATO Yasushi

Supervisors
Proffesor NAKAZAWA Masaharu
Assistant proffesor TAKAHASHI Hiroyuki

February 14, 2000

Acknowledgement

I would like to thank Dr. M.Nakazawa, Dr. H.Takahasi, Dr. K.Ishigure, Dr. M.Uesaka, Dr. S.Hasegawa, Dr. K.Kobayashi, Dr. M.Fujiwara, Dr. K.Yamahana, Dr. H.Okuma, Dr. S.Date, Dr. S.Suzuki, Dr. S.Okajima, Dr. N.Kumagai, Dr. M.Hara, Dr. Y.Kawashima, Dr. Y.Sakurai, Dr. M.Ito, Dr. H.Ego, Dr. T.Oshima, Dr. Y.Ohashi, Dr. H.Saeki, Dr. I.Nakai, Dr. H.Kamitsubo, Dr. E.E.Alp, Dr. E.S.Friedman, Dr. A.Alatas, Dr. C.E.Johnson, Dr. T.J.Wilkinson, Dr. K.A.Yener, Dr. B.Lai, Dr. G.Jennings, Dr. G.Knapp and Dr. S.M.Mini. Especially I would like to thank Dr. M.Nakazawa and Dr. H.Takahasi. They did not abandon me who did whatever I like. Finally I thank my wife Eiko for her sincere support of my life to complete doctor thesis.

Contents

Chapter 1

Introduction

Synchrotron radiation is widely used for many purposes in developing basic science. The application of laser electron photons is still at the early stage. In this chapter, synchrotron radiation and its application, laser electron photons and its application are explained. The aim of this thesis is also described briefly.

1.1 Synchrotron radiation and its application

Synchrotron radiation is a kind of the electromagnetic wave created when an electron is bend by a magnetic field. Three types of Magnet are used to generate synchrotron radiation. The first, the bending magnet is set to confine electrons in storage ring and generate continuous wavelength light from infrared rays to X-rays. The second, the wiggler magnet is set to generate light with a shorter wave length and a brighter continuous wavelength light than that with bending magnet. And the third, the undulator magnet is set to generate bright light with a particular wave length. Compared to conventional x-ray generator, synchrotron radiation has the properties of more brightness,directivity and wide range wave length.

Synchrotron radiation is used for material science, medical and biological science, and earth science. Examples of research subjects are (as is shown in table.1.1); trace element analysis, structure of atoms and moleculars electron states in material, surface structure of material, chemical reaction, catalyst, medical diagnosis ,industrial diagnosis, X-ray microscope, holography, lithography, crystal structure of materials, 3D structure of albumin, condition under high temperature and high pressure, structure of and function of muscle, structure of solution, magnetism of material, local structure of material, X-ray chemical vapor deposition and so on.

1.2 Laser electron photons (Laser synchrotron radiation)

Laser electron photons are scattered photons by electrons. When laser photons are scattered by high energy electrons, a part of electron energy is given to photons (fig. 1.1) . This process is called inverse Compton scattering. On the other hand, ordinary Compton scattering is the process that photons give the energy to electrons (fig. 1.2). We plan to generate a high flux beam of 10 MeV photons by means of collision between 8 GeV electrons and 118.8 μ m far infrared photons at SPring-8. The application of this 10 MeV photons are described in this chapter.

1.3 Application of laser electron photons

Laser electron photons(γ-ray) react with nucleus, for example ($\gamma, \gamma'\gamma''$) ,(γ, xn). The examples of applications are shown in Table 1.2.

1.3.1 Measurement of photo-nuclear reaction cross section

IAEA makes photo-nuclear reaction data base [1]. Calculational data and experimental data are accumulated systematically. BOFOB, LNDL, EPNDL, JENDL, etc are accumulated and compared in order to make high quality, no omission data base. Compared to calculated data, experiment data is limited. Experiment at SPring-8 dedicates to make this data base.

Accelerator-driven nuclear-reactor is designed in Europe and Japan to incinerate long-life fission-products. This reactor is driven by nuclear fuel and incinerate nuclear waste. Heat is changed into electric energy and at the same time long-life fission-products are incinerated. Photo-nuclear data base is needed to design the reactor.

1.3.2 Neutron source for subcritical incineration reactor

Accelerator-driven incineration-reactor is a leading candidate for long-life fission-products incineration reactor. The overview of accelerator-driven incineration-reactor is following. Accelerated protons bombard W or V targets. Neutrons are created through spallation reaction in the target. These neutrons are used to achieve reactor critical condition. Long-life fission-product nucleus is changed into short-life radioactive nucleus by fission processes.

There are some advantages when γ-rays are irradiated in the reactor and generate neutrons. A long life target which is placed on reactor center axis can serve to realize homogeneous burning distribution, because in the reactor neutron source can be placed along the

center axis of the reactor. There are no difficulty for vacuum window. Complete continuous neutron creation makes the reactor design easy.

1.3.3 Cancer therapy

BNCT (Boron Neutron Capture Therapy) had excellent record for brain cancer [3]. The method is following. ^{10}B is sent to brain cancers on BSH (^{10}B enriched sodium borocaptate) . Thermal neutron is irradiated to cancer. α particle which is produced by ^{10}B(n,α)^{7}Li reaction give the cancer fatal damage. The defect of this method is to open the head in order to irradiate thermal neutron. It is possible to make the same therapy without opening a head when photo-nuclear reactions by γ-ray can be used. But, cross section of photo-nuclear reactions is small. It is important to find materials of (γ,n) reaction with a large cross section.

1.3.4 Radiation protection

When radiograph is taken by electron linac, high energy photons are released [1]. It is important to protect from photons and also neutrons created by photo-nuclear reaction. The photo-nuclear experiment have not been enough to calculate photon transfer, photo nuclear reaction, photo-neutron reaction.

1.3.5 Nuclear fluorescence cross section

The (γ, γ') reactions on various stable isotopes have been measured by using bremsstlhung γ-rays. Some isotopes are still not measured, especially radio isotopes. Spring-8 will provide a high γ-ray flux. New fluorescence line may be found even in isotopes, which are already measured.

1.3.6 Test of nuclear model

The number of solar neutrinos which are created by hydrogen fusion process are a half of solar standard model estimation. These neutrinos are measured by β^+ decay processes of ^{37}Cl,^{71}Ga in a solar neutrinos detector. On the other hand, the flux of ^{8}B neutrinos is only about a half of the solar standard model estimation in the measurement of Super-Kamiokande. Neutrino oscillation is assumed to be the one of reasons. The pp-process and ^{8}B decay neutrinos have been detected up to now. The ^{7}Be and pp neutrinos, which is needed to solve solar neutrinos process, will be detected by ^{176}Yb, ^{160}Gd doped scintillators. This project is planed by United states, France, Germany and Japan.

(^{3}He,t) charge exchange reaction of ^{176}Yb, ^{160}Gd is measured as a part of the project[4]. It was found that spin excitation structure of these deformed nuclei had interesting systematic

feature. The spin excitation structure of a parent nuclei had relation with wave function of excitation state of residual nuclei through isospin operator. But a residual nuclei had anti analog state which do not have clear relation with the level structure of a parent nuclei. The reason of existence of anti analog state will be tried to find by precise measuring the level of parents nuclei by NRF(Nuclear Resonant Fluorescence). By the way, M1 excitation of deformed nuclei is related to IBM model, which Arima group established. M1 excitation mode of deformed nuclei is measured systematically by NRF. There are some interesting subject such as scissors mode which is the mode that neutron and proton oscillate independently like scissors.

1.3.7 Comparison with the nuclear excitation of charge exchange reaction

The spin flip excitations with a transferred angular momentum $\Delta\ell$=0 have two types; Gamow-teller excitation and M1 excitation. Gamow-teller excitation is caused by charge-exchange reactions. M1 excitation is caused by inelastic scattering. When a N=Z nuclei (T_z=0) is excited, Gamow-teller excitation states have (T_z=1), on the other hand M1 excitation states have (T=0) or (T=1). T=1 M1 excitation states is called "Isobaric analog state" of Gamow-teller excitation state. This spin flip is excited by pion exchange field. Transition matrix elements between Isobaric analog state in light nuclei is estimated by measurement of spin flip excitation and beta decay. It was measured that isospin symmetry was broken about 10 %. Isospin symmetry between excitation state was also broken . The reason will be understood by precise measurement of transition matrix for excitation state.

1.3.8 Astro-nuclear reaction

When super novae explode, large amount of neutrinos are released from the core of the star. A part of neutrinos is created by electron capture by ^{56}Fe and so on. The number of neutrinos is almost the same as the number of electrons which is in the core of the star, for example in case of SN1987 super novae, the number of electrons in the star is the order of 10^{57}. In 1987, Neutrinos from SN1987 are detected in Kamioka mine. The number of detected neutrinos represents the number of neutrinos which is created in SN1987 is much more than 10^{57}. The reason is explained as follows. Photons create electron positron pairs in high temperature and high density core. Electrons and positrons create neutrinos and antineutrinos. A large number of neutrinos are released like black body radiation at last. This assumption had coincidence with observation of neutrinos in few seconds.

The mean energy of neutrinos is about 10 MeV. These neutrinos have collision with atomic nuclei and create a large number of protons and neutrons. A part of nuclei absorbs these protons and neutrons rapidly. Then, heavy nuclei are created. The nuclei which

can be created by only this process are found in the space. Super novae is studied by calculating the abundance of these nuclei. There is the hypothesis that heavy elements like Pb in the space are created by super novae. All of heavy elements are created by r-process, which is the reaction between neutrinos and nuclei. The calculation of this model requires the knowledge of reaction cross sections between neutrinos and nuclei. However, the avalable data is not enough to explain the details of the nuclear abundance in the universe. Accurate cross sections of neutrino-nuclear reaction by neutral current will be determined by measuring accurate nuclear excited state after the reaction of neutrinos and nuclear. Systematic data of spin flip excitations on many nuclei are required for this determination.

1.3.9 Nondestructive isotope analysis

There are several methods of isotope analysis. For example, ICP-MS (Induced Coupled Plasma Mass Spectrometry), AMS (Accelerator Mass Spectrometry), etc. Mass spectrometry is used for archaeological provenance issues. Pb is appropriate elements for this purpose. Pb is the terminal nuclei of decay line. The concentration of Pb isotopes represents the age of soil.

Copper mirrors were clustered by Pb isotopes, whose ratio has the difference between the production areas [2].

But mass spectrometry is a destructive method. Archaeological samples which have artistic value can not be analyzed. Nondestructive analysis can be provided by using γ-ray. The nuclear fluorescence are measured by irradiation of γ-ray. The samples of value can be analyzed. New discovery may be expected.

1.4 Aim of this paper

From view point of element analysis, X-ray fluorescence analysis have been applied for archaeology. But the energy of incident x-rays has been low (a few tens keV). Thus heavy elements have not been examined yet. High energy synchrotron radiation can be used now. Incident X-ray energy can be increased from 100 keV up to 300 keV by SPring-8. K-absorption edges of a ll elements can be hit by these incident X-rays. Nondestructive element analysis for archaeological samples is tested using high energy synchrotron radiation.

Laser electron photons generator is developed. It consists of electron storage ring and far infrared laser system. SPring-8 is used as electron storage ring. SPring-8 was constructed and has been already used as a synchrotron radiation source. Here, development of far infrared laser is described.

Nondestructive isotope analysis have not been established yet. But laser electron photons can realize nondestructive isotope analysis. Generally valuable archaeological samples can not be scraped. Many samples are not analyzed. When nondestructive analysis can be used, these samples will be analyzed systematically.

So the aims of this thesis is three items.

- The study of nondestructive element analysis for archaeological samples using high energy synchrotron radiation
- The study of laser electron photon generator
- The study of nondestructive isotope analysis for archaeological samples using laser electron photons

Table 1.1: The application area of synchrotron radiation

Trace element analysis
Structure of atoms and molecules
Electron states in material
Structure of material's surface
Chemical reaction, Catalyst
Medical diagnosis
Industrial diagnosis
X-ray microscope
Holography
Lithography
Crystal structure of material
3D structure of albumin
Condition under high temperature and pressure
Structure and function of muscle
Structure of solution
Magnetism of material
Local structure of material
X-ray chemical vapor deposition

Table 1.2: The application area of laser electron photons

Measurement of photo-nuclear reaction cross sections
Neutron source for subcritical incineration reactor
Cancer therapy
Radiation protection
Measurement of uclear fluorescence cross section
Test of nuclear model
Comparison with the nuclear excitation of charge exchange reaction
Astro-nuclear reaction
Nondestructive isotope analysis

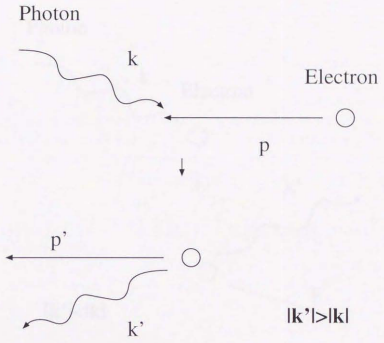

Figure 1.1: Scheme of inverse Compton scattering

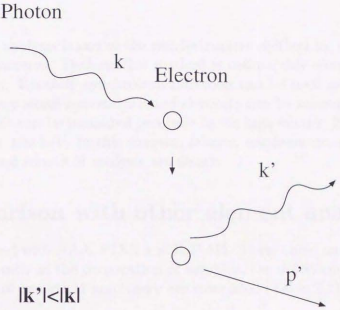

Figure 1.2: Scheme of standard Compton scattering

Chapter 2

Nondestructive element analysis

X-ray fluorescence analysis is one of the nondestructive method by which concentration of element can be measured. Because this method is comparably simple and nondestructive, it is used widely. Recently synchrotron radiation can be used as the incident X-ray probe (SR-XRF) . Very small concentration of elements can be measured by its high brilliance. Heavy elements can be measured precisely by its high energy. Spring-8 can provide 3.3×10^{13}photons/s at 100 keV. In this chapter, faience, earthenware, stoneware and sediment are measured and results of analysis are shown.

2.1 Comparison with other element analysis

SR-XRF is compared with NAA, PIXE and ICP-MS. These three methods are explained at first. Then items such as the preparation of samples, the detection limit and precision and the accessibility of analytical machinery are compared (Table 2.1).

2.1.1 NAA

In the nuclear reactor thermal neutrons are available, then radio active nuclei are produced by these thermal neutrons irradiation. The heat created by nuclear chain fission reaction is used in commercial nuclear power reactor generally, on the other hand, Thermal neutron can be taken out of research nuclear reactor. The radio active nuclei emit γ-ray radiation which can be measured and changed into the concentration of elements. The measurement is carried out after proper cooling time. The length of cooling time are decided by life time and counting rate of γ-rays. When many elements are measured, samples are measured repetitively in different cooling times.

Solid samples are analyzed generally. Volume of samples is limited because samples are put in a nuclear reactor. As to liquid samples, their small amount can be measured without

any preparation. Concentration and coagulation are needed in some cases.

2.1.2 PIXE

Charged particles such as protons, helium ions, are irradiated on samples. X-ray fluorescence from samples are measured. Small size accelerator such as a Van de graaf electrostatic accelerator is used for the PIXE studies. Electric charge is carried by a belt to the terminal, and high voltage is preserved about 2 - 3 MV. Charged particles are accelerated between this high voltage and earth. When charged particles are irradiated on atoms, excited ions are created by release of an atomic electron in a inner shell. The vacancy is occupied by an electron which occupied a higher energy level. The energy between the levels are equal to the x-ray fluorescence energy.

Solid samples are used without chemical process. Aerosol ,which is accumulated on a filter by a vacuum pomp are used without chemical process. Liquid samples are dried and put on the thin film.

2.1.3 ICP-MS

Atoms are ionized by an inductively coupled plasma. Ions are drawn into a mass spectrometer. Inductive electric field is made by high frequency current in a inductive coil. Argon gas which blow out of a quartz-triple-tube, are discharged by the electric field. The gas has three role, to form the plasma, to put up plasma in order not to touch the tube and to carry the mist of sample liquid. Mass spectrometer has two types, quadrupole type and double focus type. The quadrupole mass spectrometer consists of two pairs of two parallel electrodes which are put perpendicular to each other. Ions which have particular mass can be selected by this spectrometer. Control is simple. It scans wide mass range quickly. The double focus type achieves high resolution by static electric analyzer and magnetic sector. Interference of multi atom ions can be rejected. Control is complex. It scans slowly, but detection limit is better than that of quadrupole type.

Samples are induced as liquid solution. Solid sample are dissolved by Alkali dissolution method and acid dissolution method. Liquid samples are used without chemical process, or separation and concentration are needed in some cases.

2.1.4 Comparison with NAA, PIXE and ICP-MS

These analysis methods are compared with SR-XRF. Archaeological samples are solid, for example, rock and glass. The concentration of trace elements in samples is measured in order to solve provenance issue. The items of comparison are, preparation of sample, detection limit, precision, accessibility of these analytical machinery.

The case of preparation of samples, ICP-MS requires samples to be dissolved by acid or alkali. After dissolved, media of dissolution should be removed. Chemical process is needed. Samples are destroyed. NAA, SR-XRF, PIXE do not require chemical processing. Quantitative analysis need to form samples identically. But NAA restricts size of samples because samples are set in a nuclear reactor. SR-XRF and NAA need the samples to be identical in shape. PIXE requires the samples to be thin layer.

Detection limits of these samples is following. SR-XRF is 0.1 pg - 1 μ g. PIXE is 0.1 ng - 0.1μg. NAA is 0.01 ng - 1 μg. ICP-MS is 0.1 ng/ℓ - 1 $\mu g/\ell$.

Precision of these method is following. SR-XRF is 1%. PIXE is 1%. NAA is 5%. ICP-MS is 1%.

Accessibility of these method is following. NAA needs public facility. The beam time is limited because of other researches. Especially, the number of research reactors for NAA is decreased, for example, Rikkyo research reactor will be shut down in a few month. SR-XRF has the analysis beam lines at SPring-8. Thus, the beam time will be enough. PIXE and ICP-MS do not need to be concern time shearing when we can have private machinery.

Nondestructiveness should be taken into account at first. Broken earthenware can be scraped as in the case, but most of archaeological samples can not be scraped. Thus,ICP-MS is not appropriate because it is destructive analysis. When we can have private machinery, PIXE is the best choice because of low detection limit, high precision, no time sharing and nondestructiveness. When we can not have private machinery, SR-XRF is the best choice. PIXE needs an accelerator, and NAA needs a research reactor. The accelerator and research reactor are also used for other researches. Thus, beam time can not be assigned enough. SR-XRF has low detection limit, multi element analysis. Also SPring-8 has the analysis beam lines and long term utilization can be approved. Numbers of samples can be measured statistically in order to categorize the samples. And nondestructive isotope analysis can be realize at the same facility, SPring-8.

2.2 Faience

Faience has been made in the middle east for a long time. Figures 2.2, 2.3, 2.4 and 2.5 are pictures of faience. The way of making faience is as follows. Quartz, sand and lime are crashed into fine powder. Plant ashes and water are mixed. All of them are kneaded and shaped. They are glazed. At last, they are baked. Element analysis of faience can solve provenance issue. X-ray fluorescence analysis is applied to faience. For the first time, faience is analyzed at SPring-8. Incident X-ray is 115 keV synchrotron radiation. This energy is the absorption edge of Uranium. Lighter elements than uranium can be detected by this energy. Lanthanoid can be detected with a low background noise at this energy.

2.3 Experimental set up

The set up is shown in fig. 2.1. Synchrotron radiation bombarded on samples. The X-ray fluorescence is detected by a Ge semiconductor detector. The spectrum of fluorescence is obtained by the measurement system combined with a computer.

2.4 Results and discussion

2.4.1 Excavated faience

The faience which is excavated in Egypt and Iran are analyzed. Table 2.2 shows the faience which are analyzed. This is the first time that excavated faience is irradiated by high energy X-rays (115 keV). Figure 2.6 shows the X-ray fluorescence spectrum for a faience from Egypt. X-axis is the energy of fluorescence X-rays, and Y-axis is the counts. In this spectrum Cu, Sn, Pb, Sr, Ba, La and Ce are detected. Both the elements in glaze and basement are detected because X-rays has irradiated on both glaze and basement. Figure 2.7 shows the spectrum for the basement of a faience from Egypt. Incident X-rays are irradiated on broken face of faience. Compared to fig 2.6, the peaks Cu, Sn and Pb are shrunken. Thus, we can infer that Cu, Sn and Pb exist in glaze and Sr, Ba, La and Ce exist in basement. Materials of glaze and basement are mined from different places. Glaze are made from copper ore, basement are made from quartz, sand and lime [12]. Each places where faience are made may have each mines of these materials. When the mine of these materials are determined, it become clue of the places where faience is made.

Figure 2.8 shows the spectrum of a faience from Iran. In this spectrum, the existence of Cu, Sn, Pb, Sr, Ba, La and Ce is confirmed. Fluorescence energy of elements is shown in Table 2.3. Very small ampunt of Bi is detected only in a faience from Iran. But Bi can not be index for the production place because there are some faience in which Bi can not detected. There are possibility that the production place can be determined by the elements in the basement. Figure 2.9 shows the distribution of the faience in which X-axis is La/Ba peak ratio and Y-axis is Ce/Ba peak ratio. Faience from Egypt and faience from Iran can be classified. One of the Iran faience is in the Egypt region. It might be imported. But further analysis and accumulation of data is needed to conclude it.

La and Ce are rare earth elements. Chemical characteristics of rare earth elements are almost same. But their ion radius is different because charge in nuclei can not be obstructed by inner shell electrons. La^{3+} has the largest ion radius which is 104.5 pm, on the other hand, Lu^{3+} has the smallest ion radius which is 56.1 pm. When Rocks were changed from liquid phase into solid phase, concentration of elements were affected by the conditions of rocks and elements' ion radius. Thus, Concentration of La and Ce represents the history of their mother land.

It is difficult to determine where faience is made by analyzing by elements in glaze. The ratio of elements can be changed by colors. The ratio of elements does not represent the production place. The isotope analysis are one of promising candidates to overcome the difficulty. Both faience from Egypt and Iran had the Pb element which was used for provenance issue [2]. Thus the Pb element is chosen for Isotope analysis. On the other hand, the basement have the Ba element which has seven isotopes. And ^{138}Ba is the daughter nucleus of ^{138}La whose life time is 4.7×10^{10}. Ba isotope ratio is affected by a layer's age. The Ba element is another candidate for isotope analysis to analyze more precisely.

The Ce/Ba vs La/Ba plot is useful for classification. This means that the method can be used for provenance issue between Egypt and Iran.

2.4.2 Earthenware

Two fragments of earthenware are analyzed. Figure 2.10 shows the spectrum of small plate. Figure 2.11 shows the spectrum of a part of a bowl. These fragments have transition metals such as La, Ce, Nd, Dy, Er, Yb and Hf. Fluorescence energy of elements is shown in Table 2.4. The earthenware is made from the soil which was taken around the kiln. This means the earthenware conserves the characteristics of the soil. It is possible to solve the provenance issue by analyzing the earthenware. Figure 2.12 shows the spectrum of sand from Sudan. This spectrum has almost the same as these from Egypt. Both of them have Ba, which can be a index for isotope analysis.

2.4.3 Stoneware

The sample was excavated at "Taeki-Tanaka" remains, Okayama prefecture. It was made of tuff, 3.5cm×3.6cm×2.9cm volume (fig. 2.13). A ditch (9 mm width, 4 mm depth) is on a surface, whose color is black. High temperature might change sample's color from original gray-white to black. The age is estimated around middle of Yayoi period. (B.C.2-1). The sample is analyzed by X-ray fluorescence analysis to obtain the clue of the usage of the sample. Incident X-ray energy was 10.5 keV. The result is shown in figures 2.14 and 2.15. The X-axis is the fluorescence energy and the Y-axis is counts. Mn, Co, Fe, Ni, Cu, Zn and Ga were detected. Fluorescence energy of elements is shown in Table 2.5. Figure 2.14 shows the spectrum from the surface with a ditch. Figure 2.15 shows the spectrum from the surface with no ditch. Three measured points are on top of each other in both figures. All points in the surface with no ditch (fig. 2.15) have almost the same spectrum, which seems to be the base tuff's one. However, figure 2.14 is quite different from figure 2.15. Especially one point has rich Cu compared to Co,Zn and Ga. This rich Cu is the clue. Some archaeologists suggest this sample might be a part of mold for bronze sword. The ditch shape represents that this mold may be used for the oldest thin shape bronze sword or following middle thin shape bronze sword. However, experimental results is not enough

to conclude that this sample is a part of mold for bronze swords. Thus, further analysis is needed. Mapping or micro beam scanning is the next step to find more trace of bronze.

2.4.4 Sediment - environment change

The sediments which is excavated at the bottom of lake Golbasi in Turkey is analyzed. Lake sediments recoded the environment changes. Lake Golbasi is located at Amuq valley in the Hatay province of south central Turkey. Amuq valley is 80 - 100 m above sea level. The valley is surrounded by mountain ranges. Amonus mountain ranges lie to the west. Amonus mountain consists of igneous formations in the south and sedimentary rocks in the north. The uplands to the east and south of valley consist of denuded limestone massifs. The northeast of the valley consist of denuded basalt. The rain fall is 600 - 700 mm par a year. It's enough to cultivate the ground. Irrigation increased the crops. Three rivers flows the Amuq valley, the Kara-su from the north, the Nahr al-Afrin from the east, and the Orontes from the south. Human being have been here since 9000 years ago. Their activity have been affected by environmental changes. Down stream of Amuq valley had enough water and nutrients. There have been many lakes and marches in 30000 years. The big settlement occurred between 5000 years ago and 3000 years ago. There are some big ruins at that time. These ruins are located along the trade road which connect Syria and Mesopotamia. These ancient cities got water from springs, river and lake. The amount of water limited the farm land.

Lake Golbasi at the north end of the basin was cored by a team from Groningen University, the Netherland. The depth is 15 m. The upper 6.4 m of core was sampled for elemental analysis. Figure 2.16 is the picture of core. The concentration of trace elements in lake sediments records the environment changes. Elements are divided as 4 groups. K and Rb are categorized as clay elements. (fig. 2.17, fig. 2.18). Zr, Ti and Y are categorized as sand elements. (fig. 2.19, fig. 2.20, fig. 2.21). Ca and Sr are categorized as alkali earth elements. (fig. 2.22, fig. 2.23). Cr and Ni are categorized as metal elements. (fig. 2.24, fig. 2.25).

K and Rb represents the concentration of soils . Thus large concentration of K and Rb represents the large amount of rain falls and lake development. On the other hands, small concentration of K and Rb represents the small amount of rain falls. From 640 cm depth to 300 cm depth the concentration of K and Rb are increased. The amount of rain fall is increased at that time. After that amount of rain fall is decreased until 120 cm depth and increased again.

Zr, Ti and Y are the component of sands. The trend of them is same as K and Rb. These elements are heaped by rain fall.

The trend of concentration of Ca and Sr records the lake development and retreat. The concentration of Ca and Sr are increased between 640 cm depth and 340 cm depth. Then they are decreased rapidly. After decline they are increased slowly and make peak at 120 cm

depth. Ca is deposited as calcium carbonate salts when amount of lake water is decreased or climate is aridity. Sr has the same character. An increase of the concentration of Ca and Sr between 340 cm depth and 120 cm depth represent the increase of the concentration of calcium carbonate in the soil. At 120 cm depth the concentrations of Ca and Sr are decreased. While the concentration of K, Rb are increased. This means that an increase in K and Rb represents lake development, while an increase in Ca and Sr represents lake retreat. In both cases, the trends in these trace elements are representative of environmental change.

The source of Cr and Ni is in Amonus mountain ranges. This range has large outcrops of serpentine, the parent rock of Cr and Ni. The increased presence of Cr and Ni in the lake sediments suggests environmental degradation. The concentrations of Cr and Ni are increased from 400 cm depth up to surface.

2.5 Conclusion

Faience, earthenware, stoneware and sediment were analyzed by X-ray fluorescence analysis using synchrotron radiation. This analysis could classify faience by plotting La/Ba ratio vs Ce/Ba ratio. The changes of environment could be assumed by the trend of concentration of K, Rb, Ca, Sr, Ti, Zr, Y, Cr and Ni. The indices of isotope analysis were determined as Pb and Ba.

Table 2.1: The analysis methods

	Sample preparation	Detection limit	Precision	Accessibility of analytical machinery
ICP-MS	×	0.1 ng/ℓ - 1 μg/ℓ	- 1%	O
PIXE	O	0.1 ng - 0.1μg	- 1%	O(private) ×(public)
NAA	Δ	0.01 ng - 1 μg	- 5%	×
SR-XRF	O	0.1 pg - 1 μg	- 1%	Δ

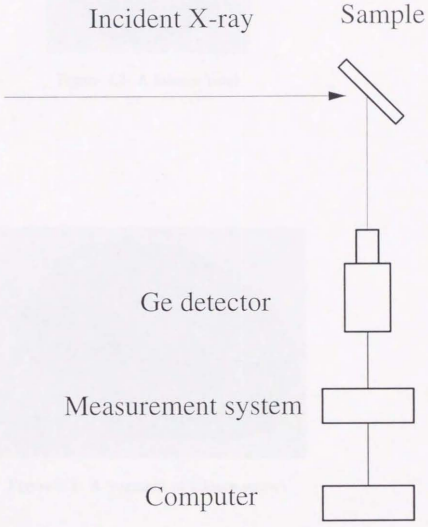

Figure 2.1: Experimental set up

Figure 2.2: A faience bead

Figure 2.3: A fragment of faience scarab

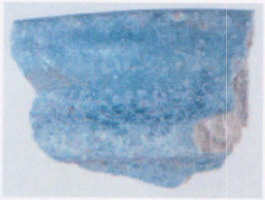

Figure 2.4: A fragment of faience bowl

Figure 2.5: Two fragment of faience udjat eye

Table 2.2: List of Faience

Name	Place	Age
A faience bead	Iran	BC 1000
A faience spin	Iran	BC 1000
A faience tube	Iran	BC 1000
Four fragments of faience udjat eye	Iran	BC 5th-4th century?
Three fragments of faience bowl	Egypt	AD 2nd century
A fragment of faience scarab	Egypt	AD 2nd century
A fragment of faience	Egypt	AD 2nd century

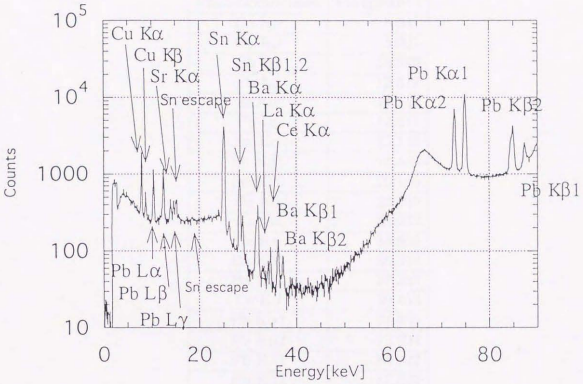

Figure 2.6: X-ray fluorescence spectrum for a fragment of faience from Egypt

Table 2.3: Fluorescence energy

Fluorescence lines	Energy[keV]
Cu Kα	8.041
Cu Kβ	8.907
Pb Lα	10.549
Pb Lβ	12.611
Sr Kα	14.142
Pb Lγ	12.611
Sn Kα	25.193
Sn Kβ1	28.483
Sn Kβ2	29.106
Ba Kα	32.065
La Kα	33.032
Ce Kα	34.569
Ba Kβ1	36.376
Ba Kβ2	37.255
Ce Kβ	39.453
Pb Kα1	74.956
Pb Kα2	72.794
Pb Kβ1	84.922
Pb Kβ2	87.343

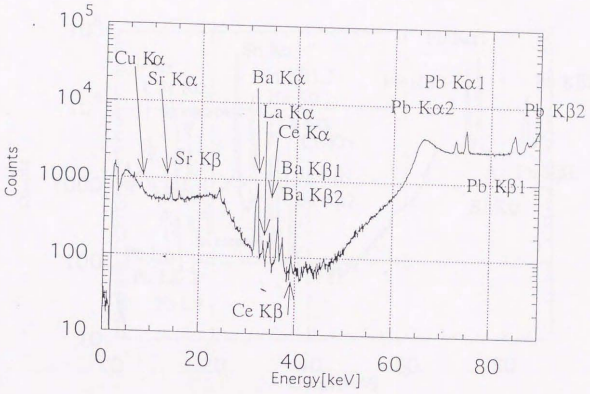

Figure 2.7: X-ray spectrum for a fragment of faience from Egypt (Basement)

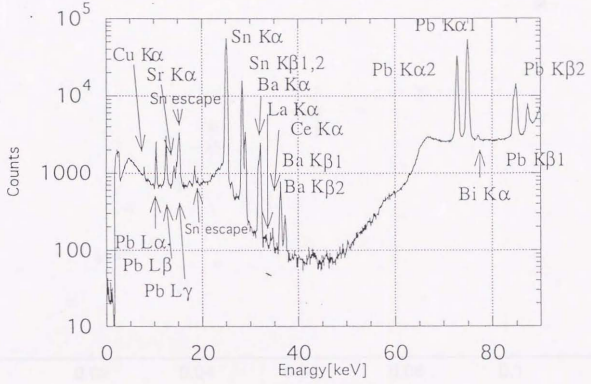

Figure 2.8: X-ray spectrum for a fragment of faience from Iran

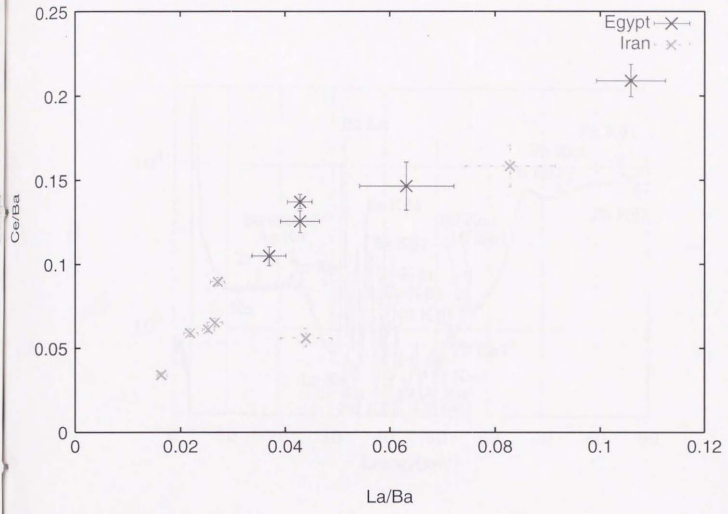

Figure 2.9: Distrubution of the faience, × Egypt faience, + Iran faience, X-axis is La/Ba peak ratio, Y-axis is Ce/Ba peak ratio

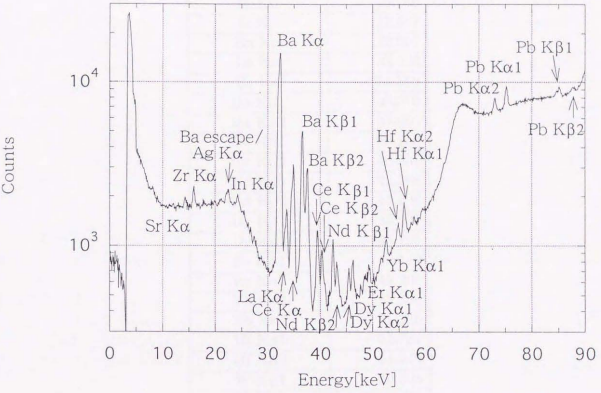

Figure 2.10: X-ray spectrum for a fragment of earthenware from Egypt (small plate)

Table 2.4: Fluorescence energy

Fluorescence lines	Energy[keV]
Sr Kα	14.142
Y Kα	14.956
Zr Kα	15.746
Zr Kβ	17.687
Ba Kα	32.065
La Kα	33.032
Ce Kα	34.569
Ba Kβ1	36.376
Ba Kβ2	37.255
Ce Kβ1	39.255
Ce Kβ2	40.231
Nd Kβ1	42.269
Nd Kβ2	43.298
Dy Kα1	45.991
Dy Kα2	45.193
Er Kα1	49.119
Er Kα2	48.205
Yb Kα1	52.380
Yb Kα2	51.326
Hf Kα1	55.781
Hf Kα2	54.579
W Kα1	59.308
W Kα2	57.973
Pb Kα1	74.956
Pb Kα2	72.794
Pb Kβ1	84.922
Pb Kβ2	87.343

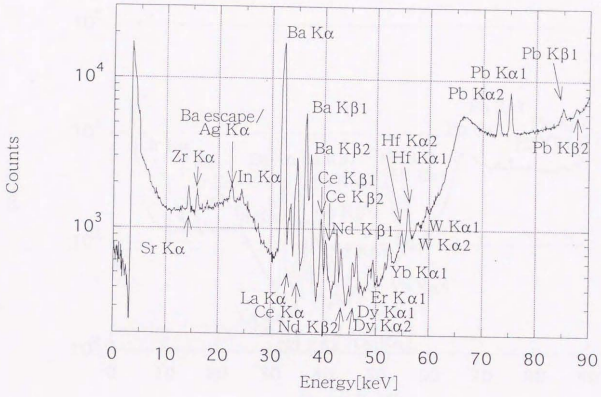

Figure 2.11: X-ray spectrum for a fragment of earthenware from Egypt (bowl)

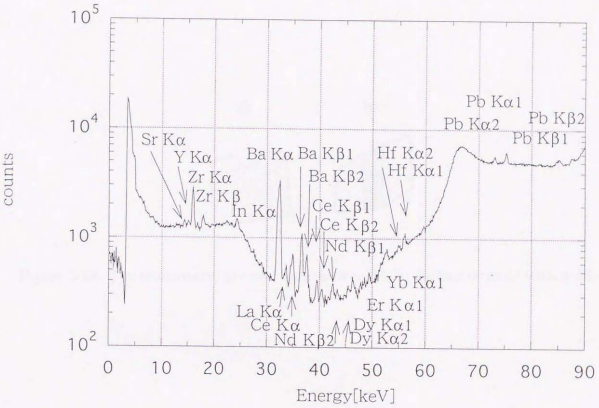

Figure 2.12: X-ray spectrum for Sand from Sudan

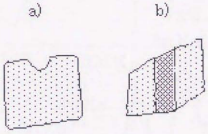

Figure 2.13: The stone ware, a) cross section of mold, b) surface of mold with a ditch

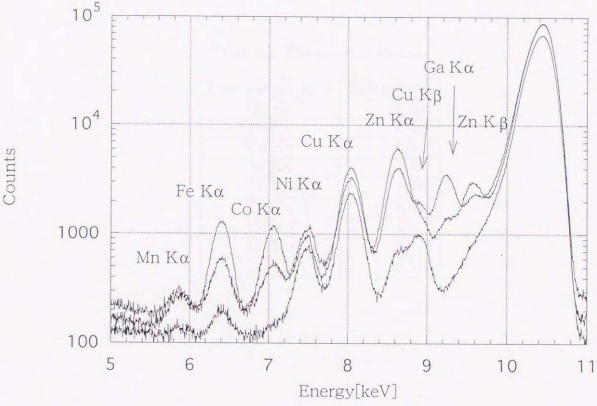

Figure 2.14: X-ray spectrum for a surface of mold

Table 2.5: Fluorescence energy

Fluorescence lines	Energy[keV]
Mn Kα	5.895
Fe Kα	6.400
Co Kα	6.925
Ni Kα	7.472
Cu Kα	8.041
Zn Kα	8.631
Cu Kβ	8.907
Ga Kα	9.243
Zn Kβ	9.572

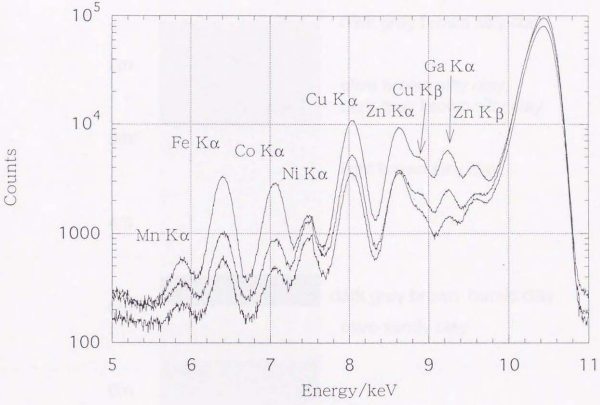

Figure 2.15: X-ray spectrum for a back side of mold

Figure 2.16: Sediment core

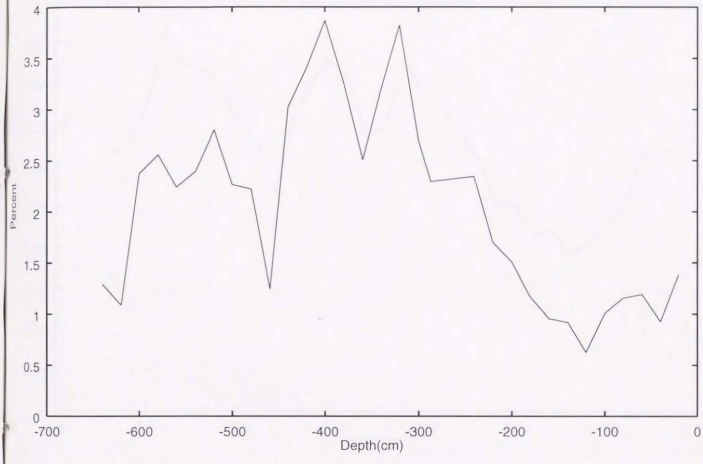

Figure 2.17: The trend of K in sediments core at lake Golbasi

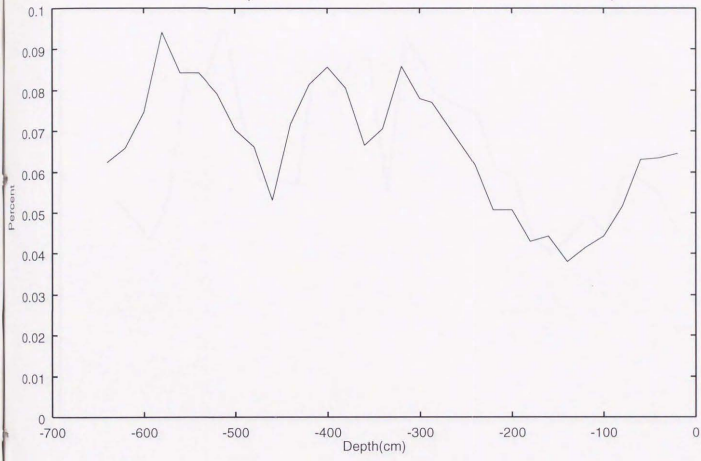

Figure 2.18: The trend of Rb in sediments core at lake Golbasi

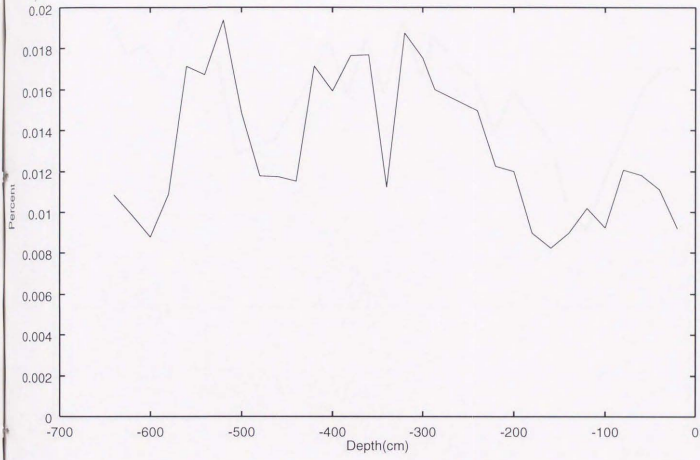

Figure 2.19: The trend of Zr in sediments core at lake Golbasi

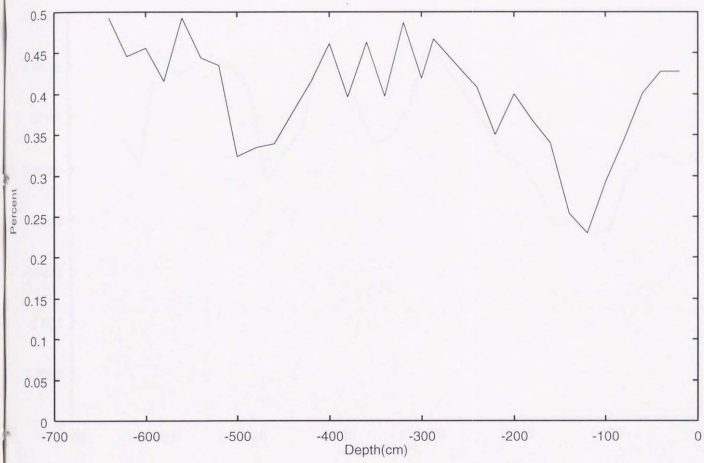

Figure 2.20: The trend of Ti in sediments core at lake Golbasi

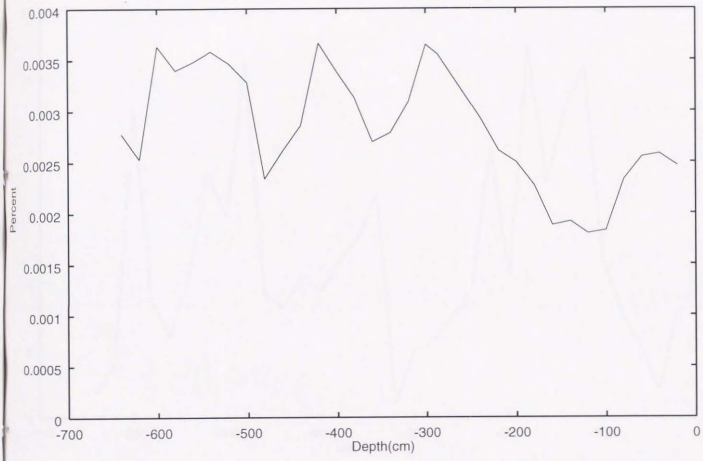

Figure 2.21: The trend of Y in sediments core at lake Golbasi

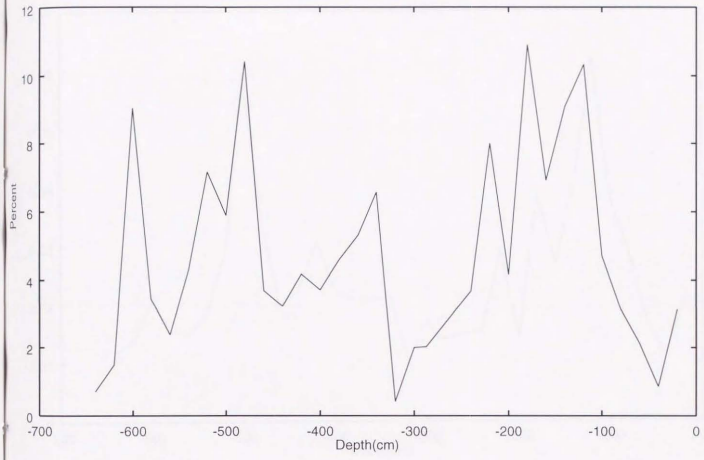

Figure 2.22: The trend of Ca in sediments core at lake Golbasi

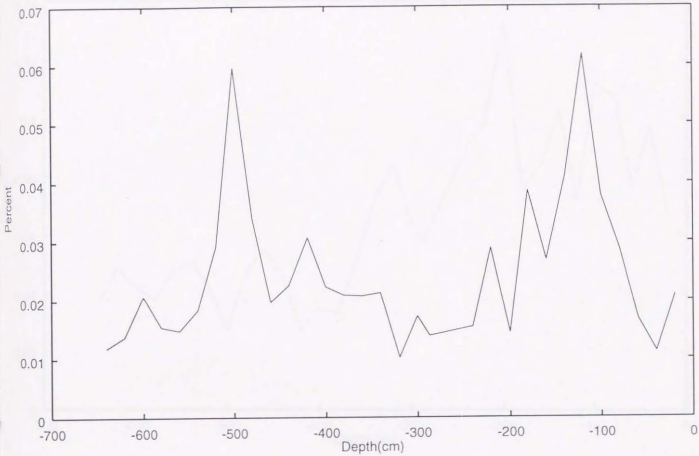

Figure 2.23: The trend of Sr in sediments core at lake Golbasi

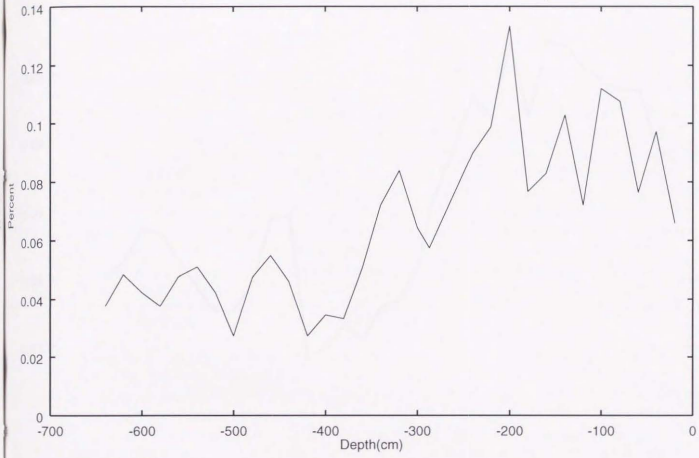

Figure 2.24: The trend of Cr in sediments core at lake Golbasi

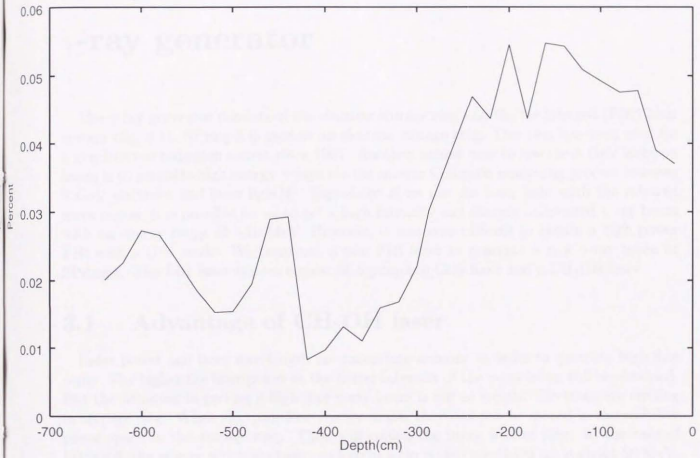

Figure 2.25: The trend of Ni in sediments core at lake Golbasi

Chapter 3

γ-ray generator

The γ-ray generator consists of the electron storage ring and the far infrared (FIR) laser system (fig. 3.1). SPring-8 is used as an electron storage ring. This ring has been used for a synchrotron radiation source since 1997. Another unique way to use the 8 GeV electron beam is to generate high energy γ-rays via the inverse Compton scattering process between 8 GeV electrons and laser light[4]. Especially, if we use the laser light with the infrared wave region, it is possible for us to get a high intensity and sharply collimated γ-ray beam with an energy range of $\sim$10 MeV. However, it was very difficult to obtain a high power FIR with a CW mode. We construct a new FIR laser to generate a new γ-ray beam at SPring-8. The FIR laser system consist of a pumping CO_2 laser and a CH_3OH laser.

3.1 Advantage of CH_3OH laser

Laser power and laser wavelength are taken into account in order to generate high flux γ-ray. The higher the laser power is, the better intensity of the γ-ray beam will be obtained. But the situation in getting a high flux γ-ray beam is not so simple. Electrons are circling in storage ring. When electrons lose energy much, they can not be stored in the stability phase space in the storage ring. They will collide the inner wall of ring. In the case of SPring-8, the energy which electron can lose in a circumference (1496 m) is about 50 MeV. The energy of electrons in SPring-8 is 8 GeV. The equation 3.32 suggests laser wave length should be longer than 24 μm. A 118.8 μm CH_3OH laser line has a strong power in this wave length region. It's power is a few or a few hundreds times higher than other laser powers (Table 3.1).

3.2 Scattering laser photons by electrons

The conservation of 4- momentum in scattering between electrons and laser is expressed as

$$p + k = p' + k'. \tag{3.1}$$

Electron's 4-momentum are p and p'. p is incoming electron's and p' is outgoing electron's. Laser photon's 4-momentum are k and k'. k is incoming photon's and k' is outgoing photon's. The parameter s, t, u are defined as,

$$s = (p + k)^2 = (p' + k')^2 = m^2 + 2pk = m^2 + 2p'k', \tag{3.2}$$

$$t = (p - p')^2 = (k - k')^2 = 2(m^2 - pp') = 2kk', \tag{3.3}$$

$$u = (p - k')^2 = (p' - k)^2 = m^2 - 2pk' = m^2 - 2p'k. \tag{3.4}$$

The Feynman diagrams of scattering between electrons and photons are shown in fig. 3.2. fig. 3.3. The scattering amplitude M_{fi} which is obtained from the Feynman diagram is given as

$$M_{fi} = -4\pi e^2 e'^*_\mu e_\nu (\overline{u} Q^{\mu\nu} u), \tag{3.5}$$

$$Q^{\mu\nu} = \frac{1}{s - m^2}\gamma^\mu(\hat{p} + \hat{k} + m)\gamma^\nu + \frac{1}{u - m^2}\gamma^\nu(\hat{p} - \hat{k}' + m)\gamma^\mu. \tag{3.6}$$

The scattering amplitude $|M_{fi}|^2$ of no polarization electrons is following.

$$|M_{fi}|^2 = 16\pi^2 e^4 tr(\rho^{(e)'}\rho^{(\gamma)'}_{\lambda\mu} Q^{\mu\nu}\rho^{(e)}\rho^{(\gamma)}_{\nu\sigma}\overline{Q}^{\lambda\sigma}), \tag{3.7}$$

where,

$$\overline{Q}_{\mu\nu} = \gamma^0 Q^+_{\mu\nu}\gamma^0. \tag{3.8}$$

The density matrices of electrons are $\rho^{(e)}$, $\rho^{(e)'}$. The density matrices of laser photons are $\rho^{(r)}$, $\rho^{(r)'}$;

$$\rho^{(r)}_{\lambda\mu} = \rho^{(r)'}_{\lambda\mu} = -\frac{1}{2}g_{\lambda\mu}, \tag{3.9}$$

$$\rho^{(e)} = \frac{1}{2}(\hat{p} + m), \tag{3.10}$$

$$\rho^{(e)'} = \frac{1}{2}(\hat{p}' + m). \tag{3.11}$$

The reaction cross section is

$$d\sigma = \frac{\pi e^4}{4}\frac{dt}{(s - m^2)^2} tr((\hat{p}' + m)Q^{\lambda\mu}(\hat{p} + m)\overline{Q}_{\lambda\mu}). \tag{3.12}$$

The reaction cross section can be written in another expression as

$$d\sigma = \frac{\pi e^4 dt}{4}(f(s,u) + g(s,u) + f(u,s) + g(u,s)), \tag{3.13}$$

$$f(s,u) = \frac{1}{4(s-m^2)^2} tr((\hat{p}' + m)\gamma^\mu(\hat{p} + \hat{k} + m)\gamma^\nu(\hat{p} + m)\gamma_\nu(\hat{p} + \hat{k} + m)\gamma_\mu), \tag{3.14}$$

$$g(s,u) = \frac{1}{4(s-m^2)(u-m^2)} tr((\hat{p}' + m)\gamma^\mu(\hat{p} + \hat{k} + m)\gamma^\nu(\hat{p} + m)\gamma_\mu(\hat{p} - \hat{k}' + m)\gamma_\nu). \tag{3.15}$$

Trace is expanded as

$$f(s,u) = \frac{2}{(s-m^2)^2}(4m^4 - (s-m^2)(u-m^2) + 2m^2(s-m^2)), \tag{3.16}$$

$$g(s,u) = \frac{2m^2}{(s-m^2)(u-m^2)}(4m^4 + (s-m^2) + (u-m^2)). \tag{3.17}$$

The reaction cross section is expanded as follows

$$d\sigma = 8\pi r_e^2 \frac{m^2 dt}{(s-m^2)^2}((\frac{m^2}{(s-m^2)} + \frac{m^2}{(u-m^2)})^2 + (\frac{m^2}{(s-m^2)} + \frac{m^2}{(u-m^2)}) - \frac{1}{4}(\frac{(s-m^2)}{(u-m^2)} + \frac{(u-m^2)}{(s-m^2)})). \tag{3.18}$$

The reaction cross section is written using x and y as

$$d\sigma = 8\pi r_e^2 \frac{dt}{x}((\frac{1}{x} - \frac{1}{y})^2 + \frac{1}{x} - \frac{1}{y} + \frac{1}{4}(\frac{x}{y} + \frac{y}{x})), \tag{3.19}$$

where,

$$x = \frac{(s-m^2)}{m^2}, \tag{3.20}$$

$$y = \frac{(m^2-u)}{m^2}. \tag{3.21}$$

The cross section differentiated by energy of out going γ-ray is,

$$\frac{d\sigma}{dE_{\gamma'}} = \frac{3\sigma_0}{|\boldsymbol{p} + \boldsymbol{k}|x}(F(x,\overline{y}) + (\frac{a}{\sqrt{a^2 - b^2}} - 1)(\frac{1}{\overline{y}^2} + \frac{\overline{y}}{4x})), \tag{3.22}$$

where,

$$F(x,\overline{y}) = (\frac{1}{x} - \frac{1}{\overline{y}})^2 + (\frac{1}{x} - \frac{1}{\overline{y}}) + \frac{1}{4}(\frac{x}{\overline{y}} + \frac{\overline{y}}{x}), \tag{3.23}$$

$$x = 2\frac{E_e}{m}\frac{E_\gamma}{m}(1 - \boldsymbol{\beta} \cdot \boldsymbol{e}_\gamma), \tag{3.24}$$

$$\overline{y} = 2\frac{E_e}{m}\frac{E_{\gamma'}}{m}\sqrt{a^2 - b^2}, \tag{3.25}$$

$$a = 1 - \beta cos\theta_{e0} cos\theta_{\gamma' 0}, \tag{3.26}$$

$$b = \beta sin\theta_{e0} sin\theta_{\gamma' 0}. \tag{3.27}$$

Coordinates are as follows.

$$\boldsymbol{e}_0 = \boldsymbol{e}_\gamma + \boldsymbol{e}_e = \begin{pmatrix} 0 \\ 0 \\ 1 \end{pmatrix}, \tag{3.28}$$

$$\boldsymbol{e}_e = \begin{pmatrix} sin\theta_{e0} \\ 0 \\ cos\theta_{e0} \end{pmatrix}, \tag{3.29}$$

$$\boldsymbol{e}_{\gamma'} = \begin{pmatrix} sin\theta_{\gamma' 0} cos\phi_{\gamma' 0} \\ sin\theta_{\gamma' 0} sin\phi_{\gamma' 0} \\ cos\theta_{\gamma' 0} \end{pmatrix}. \tag{3.30}$$

The numerical value of the Thomson scattering cross section is given as

$$\sigma_0 = \frac{8\pi r_e^2}{3} = 0.665246\ barn \tag{3.31}$$

The energy of scattered photons is

$$E_{\gamma'} = \frac{E_\gamma (1 - \boldsymbol{\beta} \cdot \boldsymbol{e}_\gamma)}{(1 - \boldsymbol{\beta} \cdot \boldsymbol{e}_{\gamma'}) + \frac{1}{\gamma_e}\frac{E_\gamma}{m}(1 - \boldsymbol{e}_\gamma \cdot \boldsymbol{e}_{\gamma'})}. \tag{3.32}$$

The number of created γ-ray photons per unit time is equal to the number of scattering between laser photons and electrons per unit time. The number of scattering between laser photons and electrons per unit time is

$$N_{scatt} = \int d^4x \frac{d^3\boldsymbol{k}}{E_\gamma}\frac{d^3\boldsymbol{p}}{E_e} c\sigma(s)\sqrt{|\boldsymbol{e}_\gamma - \boldsymbol{\beta}|^2 - |\boldsymbol{e}_\gamma \times \boldsymbol{\beta}|^2}\rho_\gamma(x,k)\rho_e(x,p), \tag{3.33}$$

where,

$$\int \frac{d^3\boldsymbol{p}}{E}\rho(x,p) = \rho(x), \tag{3.34}$$

$$\int d^3\boldsymbol{x}\rho(x) = n(t), \tag{3.35}$$

$$s = (k + p)^2, \tag{3.36}$$

$$\boldsymbol{\beta} = \boldsymbol{p}/E. \tag{3.37}$$

3.3 Flux of laser electron photons

The flux of laser electron photons are calculated by using the equation given in the former section. The parameters are laser power, laser focus position and laser focus diameter. Figure 3.4 shows the flux of laser electron photons which is the function of laser power. In this case, the laser focus diameter is 10 mm and the laser focus position is the center of scattering area. The flux of laser electron photons is about $5 \times 10^8 \sim 1 \times 10^9$ counts/MeV/s when laser power is 1 W. The flux of laser electron photons is proportional to the laser power. Since the CH_3OH laser photons do not kick out electrons, the life of stored electrons is not decreased and more laser power can be induced. The world record of the CH_3OH laser power has been 1.25 W so far. It is appropriate that the CH_3OH laser with a power of about 1 W is developed for the present purpose and the characteristics of laser power and laser electron photons are grasped. After the first achievement of us, more high power laser will be developed on the base of the successful technical development.

Figure 3.5 shows the flux of laser electron photons which is the function of laser focus diameter. In this case, the laser power is assumed to be 1 W and the laser focus position is the center of scattering area. The flux of laser electron photons is almost inversely proportional to the square of laser focus diameter.

Figures 3.6 and 3.7 show the flux of laser electron photons which is the function of laser focus position. The laser power is assumed to be 1 W and the laser focus diameter is 10 mm. The direction from the center of scattering area to laser source represent minus. The maximum flux of laser electron photons is obtained when laser focus position is on the center of scattering area.

3.4 Far infrared laser

3.4.1 Principle

CO_2 laser have many high power lines between 9 - 11 μm. Some of them excite CH_3OH molecule and oscillate far infrared laser. Figure 3.8 shows a schematic diagram of excitation. This figure shows the energy levels of CH_3OH molecular when the oscillation lines are excited by the CO_2 9P(36) laser line. The vibration level is denoted by ν. The rotation level is denoted by J. When a CH_3OH molecule is excited from a level with (ν = 0, J)

to another level with ($\nu = \nu'$, J'+1) by a CO_2 laser, inverse distribution between a level with ($\nu = \nu'$, J+1') and a level with ($\nu = \nu''$, J+1') will be realized. The laser oscillation starts with this inverse distribution. The energy between oscillating levels is in the far infrared region. Comparing to discharge excitation, CO_2 laser excitation has an advantage. Because molecules are not dissociated by the irradiation of the laser, molecular fragments do not stick on the laser oscillator tube. But the center of CH_3OH absorption lines has no coincidence with the center of CO_2 laser oscillation lines. Generally the center of the CH_3OH absorption lines locates at the slope of the CO_2 laser oscillation lines. Thus, it is important to reduce the fluctuation of the CO_2 laser frequency in order to stabilize the CH_3OH laser oscillation.

3.4.2 Pumping CO_2 laser

The CO_2 laser is a discharge excited laser (fig.3.9). The oscillator consists of discharge tubes, grating and coupler. The grating is used as wave length selector. The coupler is a half mirror by which laser is released. The piezo-electric element is placed on the couplar in order to adjust oscillator length to laser wave length. The oscillator is fixed by neocelam rods to minimize the heat expansion. The neocelam rod has a very small thermal expansion ratio (1.0×10^{-7}). The 0 th order radiation from grating, which passes through a ZnSe window, is used for monitoring and stabilization. The discharge tubes are double tubes. Discharge and oscillation arise in the inner tube. The coolant flows in the outer tube. The coolant is water usually. The temperature of coolant is controlled within accuracy of 0.1 ^{o}C. The grating and the coupler are cooled also to suppress thermal damage and thermal deformation. The discharge tube is made of Pyrex glass. Two tubes are used for the CO_2 laser. There is a gas inlet tube between them. The discharge tube holders have an aparture to cut useless oscillations with high order modes. There are adjusters both at the end and at the center of the dicharge tube for letting the discharge tube axis equal to the laser axis. This adjusting laser tube makes the laser power increase.

The CO_2 laser system was designed from the view point of reducing laser power fluctuation. CO_2 laser design precision was increased from 0.6 % to under 0.1 %. A mass flow controller is used for gas flow control instead of a valve. A power supply with high stability is used. A High precise chiller is used. The characteristics of components are shown in table 3.2.

The characteristics of the CO_2 laser are following. Parameters are, respectively, gas flow rate (N_2 gas, He gas and CO_2 gas), current, pumping speed and cooling water temperature.

Figure 3.10 shows the CO_2 gas flow rate dependence of the laser power. The condition is following. The He gas flow rate is 14.3 ℓ/min. The N_2 gas flow rate is 2.7 ℓ/min. The current is 120.4 mA. The pump speed is about 600 ℓ/min (three vacuum pumps). The cooling water temperature is 8 ^{o}C. When the CO_2 flow rate is 1.3 ℓ/min, the laser power have a maximum value of 186.0 W.

Figure 3.11 shows the N_2 gas flow rate dependence of the laser power. The condition is following. The He gas flow rate is 14.3 ℓ/min. The CO_2 gas flow rate is 1.3 ℓ/min. The current is 120.4 mA. The pump speed is about 600 ℓ/min (three vacuum pumps). The cooling water temperature is 8 $^{\circ}$C. When the N_2 flow rate is 2.6 - 2.8 ℓ/min, the laser power have a maximum value of 186.0 W.

Figure 3.12 shows the He gas flow rate dependence of the laser power. The condition is following. The N_2 gas flow rate is 2.7 ℓ/min. The CO_2 gas flow rate is 1.3 ℓ/min. The current is 120.4 mA. The pump speed is about 600 ℓ/min (three vacuum pumps). The cooling water temperature is 8 $^{\circ}$C. When the CO_2 flow rate is 1.3 ℓ/min the laser power have a maximum value of 186.0 W.

Figure 3.13 shows the current dependence of the laser power. The condition is following. The He gas flow rate is 14.3 ℓ/min. The N_2 gas flow rate is 2.7 ℓ/min. The CO_2 gas flow rate is 1.3 ℓ/min. The pump speed is about 600 ℓ/min (three vacuum pumps). The cooling water temperature is 8 $^{\circ}$C. When the current is 110 mA, the laser power have a maximum value of 186.1 W. The laser power have a maximum of value when these four parameters are changed.

Figure 3.14 shows the pump speed (the number of vacuum pumps) dependence of the laser power. A vacuum pump provide about 200 ℓ/min vacuum speed. The current and the gas flow rate are set to get a maximum laser power at any points (Table 3.3). The cooling water temperature is 8 $^{\circ}$C. The laser power is almost saturated when the number of pumps are three. The gas cost for laser power is estimated. The price of He, N_2 and CO_2 gas is shown in Table 3.4. The gas cost per 1 W is shown in Table 3.5. Thus, when the priority is laser power, three pump are used, and when the priority is cost, one pump should be used.

Figure 3.15 shows the cooling water temperature dependence of the laser power. The current and the gas flow rate are set to get maximum laser power at any points (Table 3.6). The pump speed is about 600 ℓ/min(three vacuum pumps). The laser power tend to be increased when the temperature is decreased. But too low temperature makes condensation on the laser tubes, which occurs discharge between the electric poles and the laser tubes. The prevention of discharge is needed to increase the laser power.

Figure 3.16 shows the stability of the laser power. The condition is following. Laser power is 147 W. The He gas flow rate is 9.2 ℓ/min. The N_2 gas flow rate is 1.9 ℓ/min. The CO_2 gas flow rate is 0.8 ℓ/min. The current is 100 mA. The cooling water temperature is 10 $^{\circ}$C. The pump speed is about 400 ℓ/min. The stability is about 0.5 % /h.

The laser stability affects the stability of laser electron photons flux directly. The laser electron photons flux is proportional to the density of laser photons. When the fluctuation of CO_2 laser is under 1 %/h, the fluctuation of laser electron photon flux will be %/h order.

3.4.3 CH_3OH laser

The CH_3OH laser is shown in fig. 3.17. The oscillator consists of a laser tube and a coupling mirror. The laser tube is made of Pyrex grass. The laser tube is double tube. The input coupler is an Au coated Cu mirror with a coupling hole. The output coupler is a Si hybrid coupler. The CO_2 laser reflection coating is coated on Si baseplate. The doughnut Au coating is placed on it. The doughnut coating forms an output coupling hole. The input coupler is fixed. The output coupler is located on the x stage driven by a DC motor. The oscillator is fixed by inver rods, which supress the thermal expansion. The input mirror and the output mirror are set in the vaccum chamber. The pumping CO_2 laser input window set to be the Brewster angle for the CO_2 laser. The output window is a crystal quartz etalon. The window is tilted 3° in order not to be form complexed mirror between the window and the output coupler.

3.4.4 Present status of CH_3OH laser

The record of the highest CH_3OH laser power at 118.8 μm is 1.25 W. EDINBURGE INSTRUMENTS CO. manufacture a CH_3OH laser whose laser power is less than 120 mW. What CH_3OH lasers are used for is shown in Table 3.7. CH_3OH lasers are developed for these purposes. There are some good CH_3OH lasers which have long time driving ability and frequancy stability. But laser power is not enough for our purpose. Our CH_3OH laser will have the highest laser power and also have a high stability. Laser power take priority over frequency stability because the γ-ray spectrum is a continuous spectrum. The design concept in which laser power take priority does not have been a major concept for the common usage of CH_3OH laser. Our CH_3OH laser will achieve the highest CH_3OH laser power.

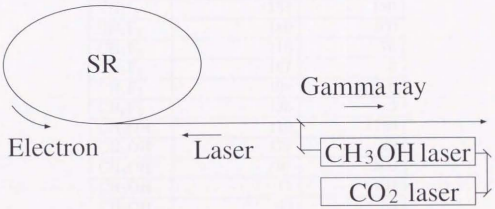

Figure 3.1: The γ-ray generator system

Table 3.1: Laser wave length and power

The optically pumped laser		
Molecules	Wave length (μ)	Power (mW)
D_2O	113	6
SO_2	140	3.5
SO_2	142	3
$^{14}NH_3$	81	40
$^{15}NH_3$	153	180
CH_2F_2	180	600
CH_2F_2	118	70
CH_2F_2	167	3
CH_2F_2	109	6
CH_2F_2	135	3
CH_3OH	119	1250
CH_3OH	171	42
CH_3OH	97	300
CH_3OH	71	102
CH_3OH	42	55
CH_3OH	65	22
CH_3OH	163	25
CD_3OD	41	60
CD_3F	190	10
The discharge pumped laser		
Molecules	Wave length (μ)	Power (mW)
H_20	28	230
H_20	119	52
HCN	337	500
DCN	190,195	1300(added)

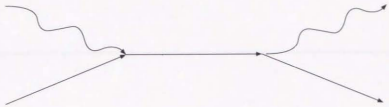

Figure 3.2: Scattering of laser photons by electrons

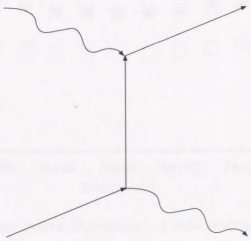

Figure 3.3: Scattering of laser photons by electrons

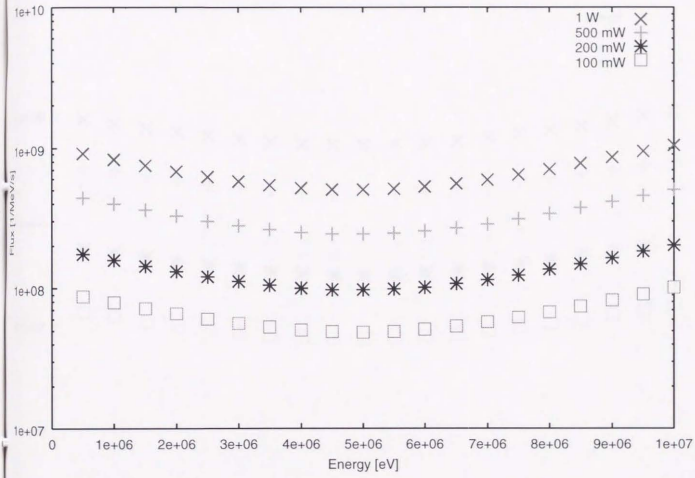

Figure 3.4: Laser power dependence of laser electron photons flux

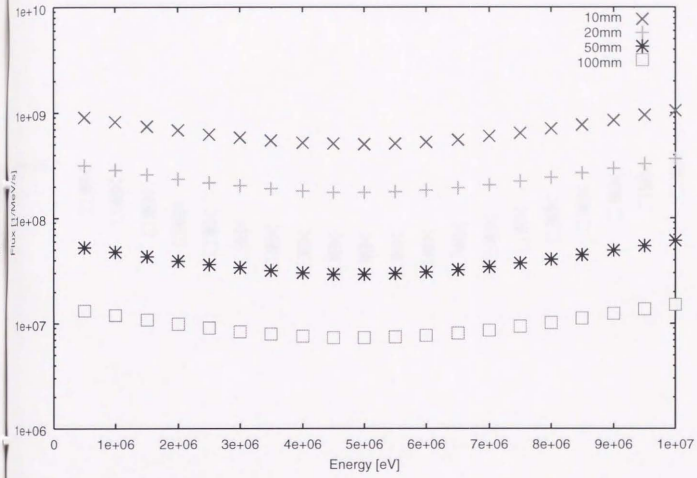

Figure 3.5: Focus diameter dependence of laser electron photons flux

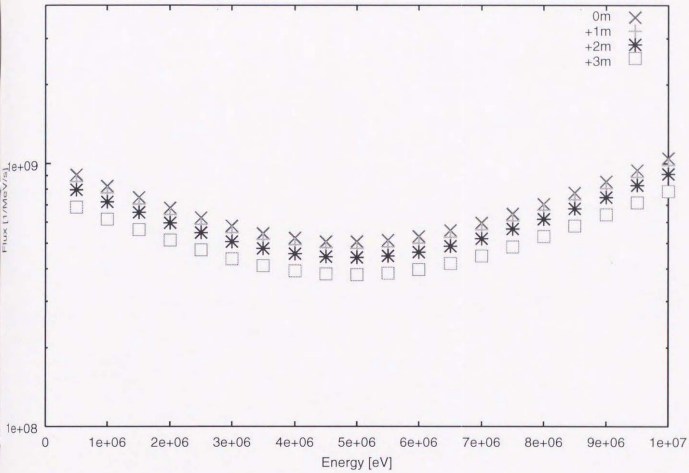

Figure 3.6: Focus point dependence of laser electron photons flux

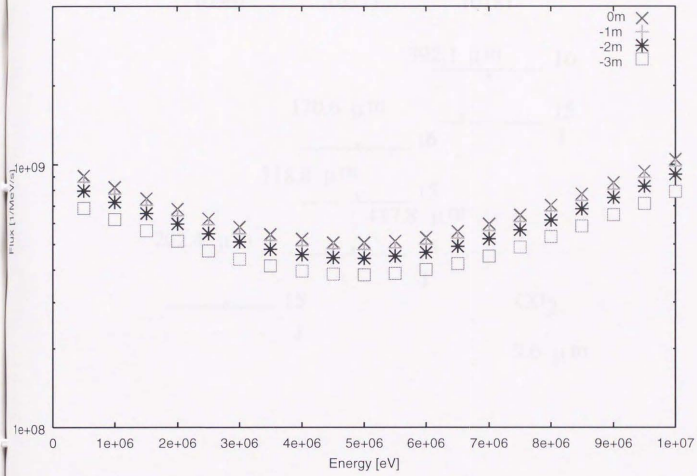

Figure 3.7: Focus point dependence of laser electron photons flux

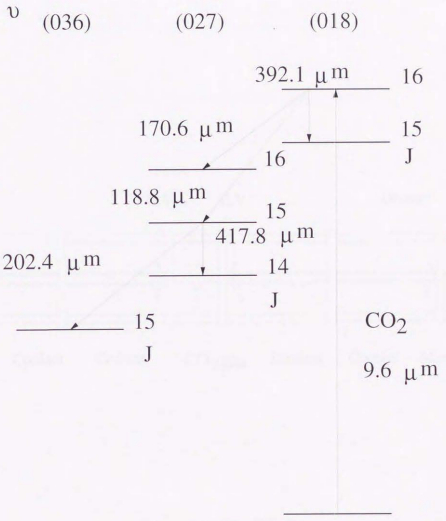

Figure 3.8: The energy levels of CH_3OH

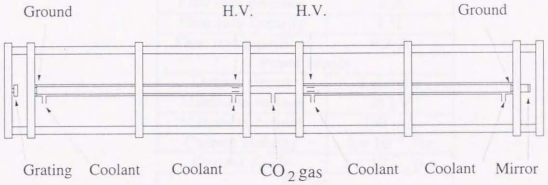

Figure 3.9: The CO_2 laser

Table 3.2: Characteristics of components

Mass flow controller	
Maximum flow rate	10 ℓ /min
Flow control range	5-100%
Flow rate precision	2 %
Flow rate linearity	1 %
Flow rate repetition	0.2 %
Power supply	
Output circuit	2 circuits
Maximum voltage	25 kV
Maximum current	150 mA
Current stability	2×10^{-3} /hr
Current ripple	2×10^{-3} /p-p
Chiller	
Temperature range	5 - 35 ^{o}C
Temperature precision	0.1 ^{o}C
Cooling power	10000 W(20 ^{o}C)
Tank volume	50 ℓ

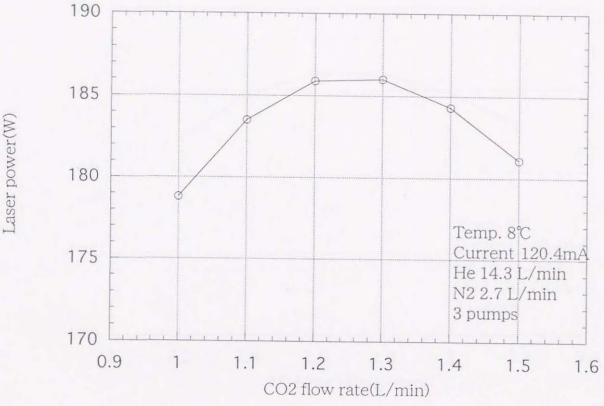

Figure 3.10: The CO_2 flow rate dependence of laser power

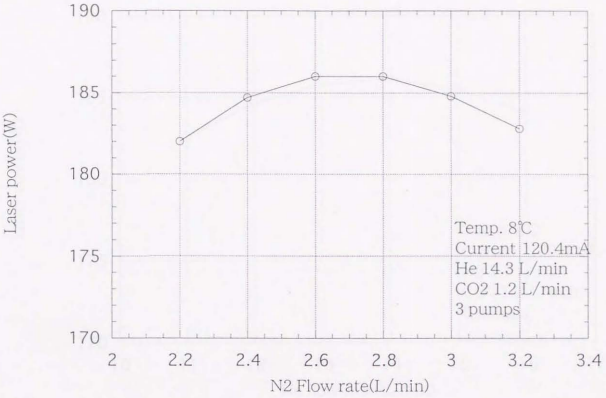

Figure 3.11: The N_2 flow rate dependence of laser power

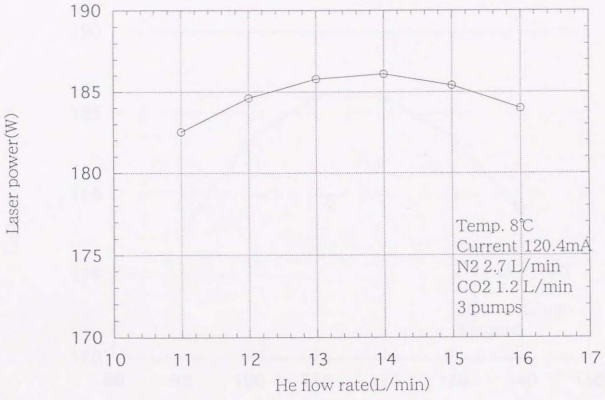

Figure 3.12: The He flow rate dependence of laser power

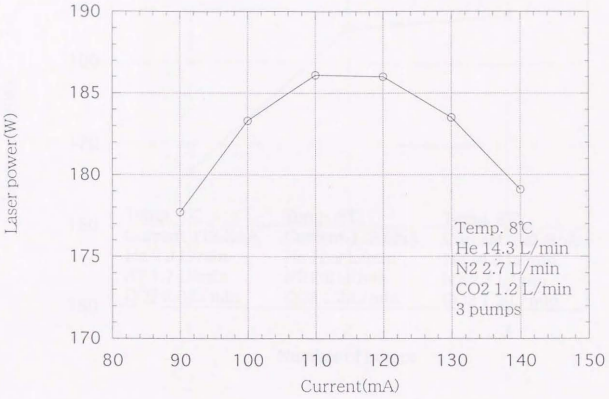

Figure 3.13: The current dependence of laser power

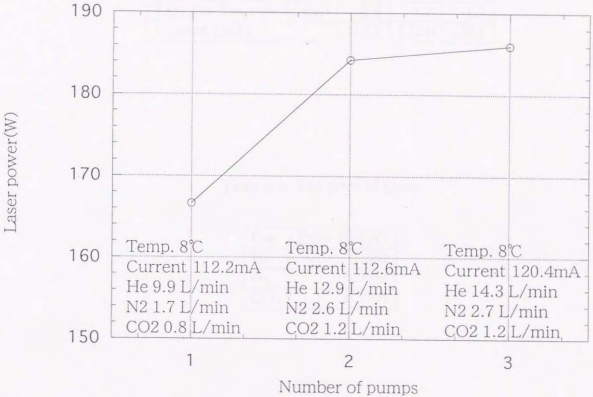

Figure 3.14: The pump speed (number of pumps) dependence of laser power

Table 3.3: The conditions of gas and current

Number of pumps	1	2	3
He gas flow rate(ℓ/min)	9.9	12.9	14.3
N_2 gas flow rate(ℓ/min)	1.7	2.6	2.7
CO_2 gas flow rate(ℓ/min)	0.8	1.2	1.2
Current (mA)	112.2	112.6	120.4

Table 3.4: The price of gases

Gas	Price (yen/ℓ)
He	1.560
N_2	0.3000
CO_2	0.3663

Table 3.5: The gas cost

Number of pumps	1	2	3
Gas cost (yen/W)	1.626×10^{-3}	1.932×10^{-3}	2.113×10^{-3}

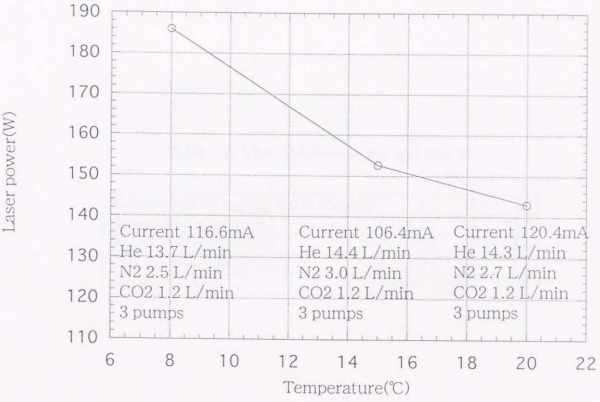

Figure 3.15: The cooling water temperature dependence of laser power

Table 3.6: The conditions of gas and current

Temperature of cooling water (degree)	8	15	20
He gas flow rate(ℓ/min)	14.3	14.4	13.7
N_2 gas flow rate(ℓ/min)	2.7	3.0	2.5
CO_2 gas flow rate(ℓ/min)	1.2	1.2	1.2
Current (mA)	120.4	106.4	116.6

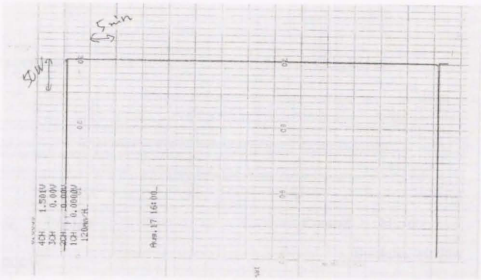

Figure 3.16: The stability of laser power

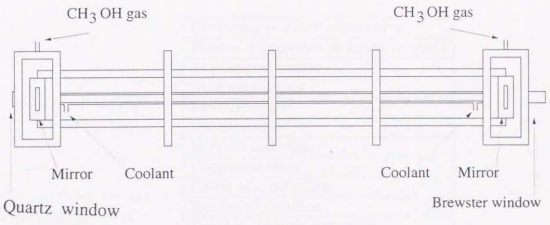

Figure 3.17: The CH_3OH laser

Table 3.7: The application of CH_3OH laser

Cycrotron resonant absorption
Plasma diagnostics in fusion reactors
Atmospheric studes
Nonlinear optics
Interferometry
Spectroscopy
Infrared astronomy
Communication
Radar and detection
Testing of detector
Uranium isotope seperation

Chapter 4

Nondestructive isotope analysis

4.1 Introduction

The isotope analysis have been made by means of mass spectroscopy such as, ICP-MS, AMS. The principle of ICP-MS is given as follows. Isotopes are ionized by inductively coupled plasma. Ions are guided into a mass spectrometer. In case of AMS, isotopes are ionized by sputtering. Ionized isotopes are accelerated by accelerator, such as tandem accelerator, and isotopes are analyzed by a mass spectrometer. ICP-MS can analyze many isotopes quickly. AMS can measure the isotope ratio with a high sensitivity. The new method (LEP-NF, Laser Electron Photons-Nuclear Fluorescence) will have low sensitivity and is slow measurement but nondestructive (table 4.1).

Mass spectrometry is a destructive method. Because a very small amount extracted from a sample can be used, ICP-MS and AMS are said to be almost nondestructive. But there is no method, which is completely nondestructive, which does not require to scrape samples. Archaeological samples can not be destroyed. Development of nondestructive analysis is requested. In this chapter, nondestructive isotope analysis using laser electron photons are described.

4.2 Isotopes as indices

Advantages of using lead and barium are taken into account. Lead is contained by glaze of faience and bronze. ^{206}Pb is decay terminal of ^{238}U whose life is 4.47×10^{9} years. ^{207}Pb is decay terminal of ^{235}U whose life is 7.04×10^{8} years. ^{208}Pb is decay terminal of ^{232}Th whose life is 1.4×10^{10} years. The isotope ratios of them, for example, ^{207}Pb/^{206}Pb and ^{208}Pb/^{206}Pb are affected by the age of ore. Thus these isotope ratios can be the indices of provenance.

Barium is contained in the basement of faience and earthenware. ^{138}Ba is a daughter

nucleus from ^{138}La whose life time is 9.87×10^{10} years. The isotope ratio of ^{138}Ba/^{137}Ba is affected by the age of ore. Thus this isotope ratio can be the indices of provenance.

4.3 Experimental set up

Measurement of fluorescence is following. Laser electron photons are bombarded on samples. Fluorescence γ-rays are measured by a Compton suppressed Ge detector. A energy spectrum is taken by measurement system and computer. Fluorescence amplitude is changed into the isotope ratio.

4.4 Nuclear fluorescence

The number of nuclear fluorescence par unit time is,

$$N = I\sigma\rho x. \tag{4.1}$$

N is Number of nuclear fluorescence par unit time, I is laser electron photons flux, σ is cross section, ρ is sample density and x is sample thickness.

The energy and number of nuclear fluorescence of ^{206}Pb, ^{207}Pb, ^{208}Pb, ^{137}Ba, ^{138}Ba, are shown in table 4.2, 4.3, 4.4, 4.5 and 4.6, respectively. In this case, sample is 100% pure isotope, 1 mm thick and laser electron photon flux is $\sim10^9$ photons/MeV/s.

In case of bronz sample, sample thickness is $\sim$1 cm, $\sim$5 % Pb is containd. Detector's efficiency is 0.1 %. Compared to 100% pure isotope sample, detection efficiency assumed to be 10^{-4}. Thus, $\sim$10 counts/s counting will be obtained. Measurement precision 0.3 % can be obtained in 10^4s. This method can be realized.

In case of faience glaze, sample thickness is $\sim$0.1 mm, $\sim$1 % Pb is containd. Detector's efficiency is 0.1 %. Compared to 100% pure isotope sample, detection efficiency assumed to be 10^{-7}. Thus, $\sim10^{-2}$ counts/s counting will be obtained. In case of faience basement, sample thickness is $\sim$1 cm, $\sim$0.1 % Ba is containd. Detector's efficiency is 0.1 %. Compared to 100% pure isotope sample, detection efficiency assumed to be 10^{-6}. Thus, $\sim10^{-2}$ counts/s counting will be obtained. These countings are too few for measurement. More laser electron photons flux is needed. When laser cavity will be introduced, laser electron photons flux will be hundreds or thausands times higher. Then faience can be measured.

4.5 Conclusion

The method and realization of nondestructive isotope analysis for archaeological samples using laser electron photons were described.

	Destructiveness	Sample condition	Detection limit
ICP-MS	Destructive	Solution	1e-2
AMS	Destructive	Cathode	1e-16
LEP-NF	Nondestructive	No processing	NA

Table 4.1: Isotope analysis method

Table 4.2: The energy and number of nuclear fluorescence of ^{206}Pb

^{206}Pb		
Energy[keV]	Cross section[eV·b]	Fluorescence[s^{-1}]
1.704	1.5e+03	5.1e+03
3.742	4.2e+03	1.4e+04
4.114	8.1e+03	2.7e+04
4.326	2.2e+04	7.3e+04
4.602	4.9e+03	1.6e+04
4.975	1.5e+04	4.9e+04
5.040	2.9e+04	9.5e+04
5.578	7.3e+03	2.4e+04
5.646	1.4e+04	4.7e+04
5.690	7.0e+03	2.3e+04
5.799	1.4e+04	4.5e+04
5.855	4.0e+04	1.3e+05
5.903	5.7e+04	1.9e+05
6.731	5.5e+04	1.8e+05
6.841	7.2e+04	2.4e+05
7.550	7.2e+04	2.4e+05
7.960	3.6e+04	1.2e+05

Table 4.3: The energy and number of nuclear fluorescence of ^{207}Pb

^{207}Pb		
Energy[keV]	Cross section[eV·b]	Fluorescence[s^{-1}]
4.871	2.3e+04	7.6e+04
4.981	2.4e+04	8.1e+04
5.223	1.4e+04	4.6e+04
5.489	5.7e+04	1.9e+05
5.596	4.4e+04	1.4e+05
5.611	2.7e+04	8.8e+04
5.690	1.4e+04	4.6e+04
5.714	2.9e+04	9.5e+04
5.734	2.4e+04	7.8e+04
5.794	1.1e+04	3.6e+04
6.179	1.3e+04	4.3e+04
6.542	8.2e+03	2.7e+04
6.735	9.0e+03	3.0e+04
6.749	2.4e+04	7.9e+04
6.818	1.7e+04	5.5e+04
7.306	8.5e+03	2.8e+04

Table 4.4: The energy and number of nuclear fluorescence of ^{208}Pb

^{208}Pb		
Energy[keV]	Cross section[eV·b]	Fluorescence[s^{-1}]
4.085	4.5e+03	1.5e+04
4.842	3.3e+04	1.1e+05
5.293	2.8e+04	9.1e+04
5.512	1.1e+05	3.7e+05
5.846	5.3e+03	1.8e+04
5.948	4.3e+03	1.4e+04
6.264	1.0e+04	3.3e+04
6.312	1.2e+04	4.0e+04
6.363	6.0e+03	2.0e+04
6.721	2.6e+04	8.4e+04
6.980	8.1e+02	2.7e+03
7.064	5.8e+04	1.9e+05
7.084	2.8e+04	9.0e+04
7.243	4.9e+03	1.6e+04
7.278	4.9e+03	1.6e+04
7.332	7.6e+04	2.5e+05

Table 4.5: The energy and number of nuclear fluorescence of ^{137}Ba

^{137}Ba		
Energy[keV]	Cross section[eV·b]	Fluorescence[s^{-1}]
3.072	6.4e+02	9.8e+02

Table 4.6: The energy and number of nuclear fluorescence of ^{138}Ba

^{138}Ba		
Energy[keV]	Cross section[eV·b]	Fluorescence[s^{-1}]
1.436	1.7e+02	2.6e+02
2.218	1.2e+02	1.9e+02
2.640	2.4e+01	3.6e+01
3.338	1.3e+02	1.9e+02
3.365	8.7e+01	1.3e+02
3.643	8.6e+01	1.3e+02
4.027	2.5e+03	3.8e+03
4.326	1.2e+02	1.8e+02
4.448	3.3e+02	5.1e+02
4.857	1.3e+03	1.9e+03

Chapter 5

Conclusion

Three topics were described on this thesis,

- The study of nondestructive element analysis using high energy synchrotron radiation,
- The study of laser electron photons generator,
- The study of nondestructive isotope analysis using laser electron photons.

In this work of nondestructive element analysis using high energy synchrotron radiation, faience and earthenware were measured at first time. And stoneware and sediment were measured also. Heavy elements were measured well by using Kα lines. Provenance issue of faience between Egypt and Iran could be solved by plotting the La/Ba ratio vs Ce/Ba ratio. It was found that lanthanoid is appropriate index for provenance issue. The changes of environment could be assumed by the trend of concentration of K, Rb, Ca, Sr, Ti, Zr, Y, Cr and Ni. The indices of isotope analysis were determined as Pb and Ba.

Concerning the work on laser electron photons generator, spectrums of laser electron photons were calculated and a new development for the highest laser power of the far infrared laser were described. The best condition of laser electron photons generation was explored. The design of the CO_2 laser and the CH_3OH laser was described. The characteristics of the CO_2 laser were measured and were described.

For nondestructive isotope analysis, a new method of isotope analysis of lead and barium using laser electron photons was proposed.

Bibliography

[1] T. Fukabori, IAEA/CRP the second meeting of accumuration and estimation of photo-nuclear reaction data.

[2] H. Mabuchi, The meeting of conservation science, p.37, (1986).

[3] K. Amemiya et al, The proceedings of japanese nuclear society,(1999).

[4] M. Fujiwara et al, Acta Phys. Pol. B, Vol.29, p.141, (1998).

[5] H. Kurosawa , Laser research, Vol.21, No.1, p.229, (1993).

[6] S. Date, private communication.

[7] S. Okajima, Solid physics, Vol.31, No.4, p.327, (1996).

[8] Y. Naito, Master thesis, Chubu University, (1993)

[9] J. Farhoomand and H. M. Picdett, Int. J. Infrared and Millimeter Waves , No.5, Vol.8, p.441, (1987).

[10] Masanobu Yamanaka, J. Opt. Soc. Am, Vol.67, No.7, p.952, (1977).

[11] M. Fujiwara et.al. Nucl. Phys. A599, p.223, (1996).

[12] S. M. Goldstein, Pre-roman and Early Roman glass in The Corning Museum of Glass, Coring. New York, p.9, (1979)

[13] M. Fujiwara et al., Jounal of the Japanese society for Synchrotron Radiation Research, Vol.10, p.23, (1997).

[14] H. Okuma, Desertation for TMU.

[15] D. Veron et al., Infrared Phys. Vol.18, p.465, (1978).

[16] Ch. sturzenegger et al., Infrared Phys. Vol.19, p.277, (1979).

[17] M. Yamanaka, J. opt. Soc. Amer. Vol.67, No.7, p.952, (1977).

[18] S. Okajima et al., Infrared Phys. Vol.25, No.3, p.569, (1985).

[19] R. Leicht et al., Nucl. Phys. A362, p.111, (1981).

[20] P. Christillin, J. Phys. G: Nucl. Phys. 12, p.837, (1986).

[21] K. Nomoto et al., Nucl. Phys. A621, p.467, (1997).

[22] K. Nomoto et al., Nucl. Phys. A616, p.79, (1997).

[23] M. Hashimoto, Astron. Astrophys. 210, L5, (1989).

[24] M. Hashimoto et al., Publ. Astron. Soc. Japan, 35, p.1, (1983).

[25] S.Okajima et al., Infrared Phys. Vol.25, No.3, p.569, (1985).

[26] R. D. Herzberg, Nucl. Phys. A592, p.211, (1995).

[27] N. Nord et al., Phys. Rev. Vol.54, No.5, p.2287, (1996).

[28] N. Pietralla et al., Phys. Rev. Lett. Vol.73, No.22, p.2962, (1994).

[29] N. Pietralla et al, Nucl. Phys. A618, p.141, (1997).

[30] W. Geiger et. al. Nucl. Phys. A580, p.263, (1994).

[31] N. Pietralla et al., Phys. Lett. B349, p.1, (1995).

[32] N. Pietralla et al., Phys. Rev. C, Vol.52, No.5, R2317, (1995).

[33] N. Pietralla et al., Phys. Rev. C, Vol.51, No.2, p.1021, (1995).

[34] H. Maser et al., Phys. Rev. C, Vol.54, No.5, R2749, (1996).

[35] H. Maser et al., Phys. Rev. C, Vol.53, No.6, p.2749, (1996).

[36] P. Brentano et al., Phys. Rev. Lett Vol.76, No.12, p.2029, (1996).

[37] R. Moreh et al., Phys. Rev. C, Vol.50, No.4, p.2222, (1994).

[38] J. Margraf et al., Phys. Rev. C, Vol.52, No.5, p.2429, (1995).

[39] F. Thielemann et al., Astro. J , 349, p.222, (1990).

[40] N. Pietralla et al., Phys. Rev. C, Vol.58, No.1, p.1, (1998).

[41] I. Wiedenhoever et al., Phys. Rev. C, Vol.56, No.5, R2354, (1997).

[42] R. D. Herzberg et al., Phys. Lett. B, 390, p.49, (1997).

[43] T. Nakazato et al., Phys. Rev. Lett. Vol.63, No.12, p.1245, (1989).

[44] V. N. Litvinenko et al., Phys. Rev. Lett. Vol.78, No.24, p.4569, (1997).

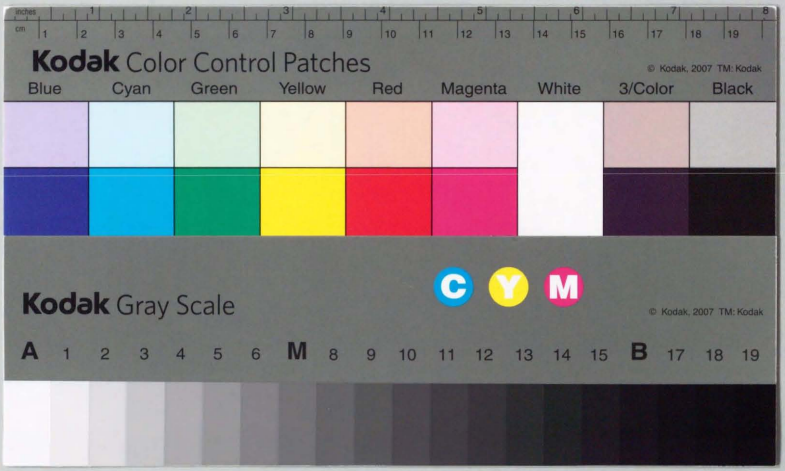
inches
cm
Kodak Color Control Patches
© Kodak, 2007 TM: Kodak
Blue
Cyan
Green
Yellow
Red
Magenta
White
3/Color
Black
Kodak Gray Scale
C
Y
M
© Kodak, 2007 TM: Kodak
A 1 2 3 4 5 6 M 8 9 10 11 12 13 14 15 B 17 18 19